

Unveiling the medium-range order in glass models and its role in glass formation

Xinyu Fan^{1,2}, Yang Sun^{3,4}, Cai-Zhuang Wang,^{3,*} Kai-Ming Ho,³ M. S. Altman,² and Li Huang^{1,†}

¹Department of Physics, Southern University of Science and Technology, Shenzhen, Guangdong 518055, China

²Department of Physics, Hong Kong University of Science and Technology, Clear Water Bay, Kowloon, Hong Kong SAR, China

³Ames Laboratory, U.S. Department of Energy and Department of Physics, Iowa State University, Ames, Iowa 50011, USA

⁴Department of Applied Physics and Applied Mathematics, Columbia University, New York, New York 10027, USA



(Received 15 January 2020; revised manuscript received 10 May 2020; accepted 20 May 2020;
published 4 June 2020)

The correlation between structure and glass formability in glassy systems is a long-standing puzzle. To solve this puzzle, many descriptors based on the short-range order (SRO) have been proposed. Here we show that the SRO, however, offers little help in explaining the glass formability and stability; instead it is the formation of medium-range order that stabilizes the glass against crystallization by suppressing the atomic rearrangement and compositional change. Our results provide a perspective for understanding the correlation between structure and stability in glasses.

DOI: [10.1103/PhysRevB.101.214104](https://doi.org/10.1103/PhysRevB.101.214104)

I. INTRODUCTION

A considerable effort has been devoted to studying the relationship between the structures and properties in glassy systems over the last few decades, during which a plethora of local-order-based analysis methods have been proposed [1]. Though these methods provide useful insights into the nature of glassy systems, a systematical assessment shows that the short-range order (SRO) description of glass is at least insufficient to clarify the glass formability (GFA) and stability [2]. Although it has been strongly suggested that the icosahedral short-range order (SRO) can be a critical factor in preventing the crystallization in many model and real systems [3–7] because icosahedra cannot tessellate the dimensional space without distortion, some recent studies suggest that local icosahedral order may not necessarily lead to glass formation [8,9].

Besides SRO, the medium-range orders (MROs) in glasses also draw intensive research interest [10–13]. The medium-range crystalline order has been proven to be strongly correlated with dynamic heterogeneity and slowdown in two-dimensional (2D) hard-disk liquids [14,15]. In three-dimensional (3D) systems, different models were proposed to characterize the MRO, including the connected quasiequivalent clusters [16,17], the fractal dimension packing [18–20], and the persistent diagram method borrowed from data science [21], to name a few. However, a robust order parameter that can give an accurate description of MRO is still inconclusive, and the conclusions drawn from 2D systems are not yet fully validated in 3D systems. Nevertheless, implicit connections between MRO and glass properties have been observed in many studies [22–24]; e.g., lower cooling rate can lead to more pronounced MRO as well as superior stability in

glass samples. It is thus critical to explore the explicit form of MRO, and its role in glass formability and stability.

In this article, we study the critical role of MRO in glass formability against crystallization by comparing two model systems which exhibit marginal difference in SRO but significant difference in MRO, and particularly different glass formability. By analyzing the detailed structural order at the medium range, we show that MRO with fivefold symmetry can emerge well beyond the first atomic shell in the glass-forming model, which hinders its crystallization.

II. METHODS

One of the models in our study is the well-known Kob-Andersen (KA) model for a binary Lennard-Jones (LJ) mixture [25], with the following parameters: $\epsilon_{AA} = 1.0$, $\epsilon_{BB} = 0.5$, $\epsilon_{AB} = 1.5$, $\sigma_{AA} = 1.0$, $\sigma_{BB} = 0.88$, and $\sigma_{AB} = 0.8$. The other model is a modified KA (MKA) system, where the *B-B* interaction strength is doubled from that in the KA model; i.e., $\epsilon_{BB} = 1.0$. All the parameters in both models are in the LJ reduced units. Both systems contain 4000 atoms with composition of $A_{80}B_{20}$, where *A* and *B* denote the larger and smaller particles; and the periodic boundary conditions are applied in all the directions. The molecular dynamics (MD) simulations are performed using the LAMMPS package [26], with the isothermal-isobaric ensemble (*NPT*) using the Nosé-Hoover thermostat and a time step of $2 \times 10^{-3} \tau$. The external pressure was fixed to 0 for all MD runs. The SRO and MRO are analyzed using the trajectories from the MD simulations and the cluster-alignment method [27,28]. The two systems are first equilibrated at $T = 0.8$ which is well above the melting point, followed by the quenching to $T = 0.2$. The inherent structures obtained by fast quenching to $T = 0.01$ were adopted throughout the study. Most of the data were collected from five independent runs unless otherwise specified.

*wangcz@ameslab.gov

†huangl@sustech.edu.cn

III. RESULTS AND DISCUSSIONS

Figure 1(a) shows the potential energy of the two models as a function of temperature during quenching at a high cooling rate of 1×10^{-5} . One can see that both the KA and MKA systems undergo glass transition; the glass-transition temperature (T_g) is around 0.33 estimated from the change of the slope in the potential energy vs temperature curve. However, when using a lower cooling rate of 1×10^{-7} , the KA system still shows a glass transition, while the MKA system crystallizes, as indicated by the sudden drop of the potential energy shown in Fig. 1(b). To further verify the glass stability, the KA and MKA glass samples generated by the high cooling rate are annealed at a temperature slightly higher than T_g . One can see the MKA glass sample crystallizes quickly while the KA sample shows almost no change for quite a long time, as evidenced in Fig. 1(c). Previous studies have revealed that the KA system is also a poor glass former at large system size [29]; it is thus necessary to check whether the difference in GFA between the KA and MKA systems is caused by the finite size effect. For this purpose, we perform MD simulations for both systems with $N = 16\,000$ and the cooling rate being 1×10^{-5} and 1×10^{-7} . To save some computational time, the MD simulations for larger systems are performed in a narrower temperature window. For a cooling rate of 1×10^{-5} , both larger systems still vitrified; thus only the results for 1×10^{-7} were presented in Fig. 1(d). At the cooling rate of 1×10^{-7} , the larger KA and MKA systems show behaviors similar to the smaller counterparts, indicating that the differences in GFA between KA and MKA are similar for systems with different sizes; hence we focus on $N = 4000$ in the remaining work.

The pair-correlation functions (PCFs) and partial PCFs of KA and MKA liquid and glass samples are presented in Fig. 1(e). The differences between PCFs of KA and MKA are defined as $\Delta g(r) = g(r)_{\text{KA}} - g(r)_{\text{MKA}}$ and are inserted under the PCFs. The magnitude of $\Delta g(r)$ is small compared to the PCFs except for that of *B-B*, which is reasonable since the interaction strength for *B-B* is doubled in the MKA model. The most pronounced peaks of $\Delta g(r)$ emerge around the first peak of $g(r)$, suggesting that the PCFs of MKA are merely shifted a little bit compared to that of KA. This shift corresponds to the changes in SRO bond lengths. In this case, the average bond length of SRO clusters in MKA is shortened. This is later confirmed by the chemical order analysis, where the SRO in KA and MKA is proved to be $A_{10}B_1$ and $A_{9.33}B_{1.67}$, respectively. The *B-B* bond lengths are smaller than other bonds; thus the peaks of the PCFs move slightly to the left in the MKA system. Hence the two models with very different glass formabilities essentially show similar PCFs in their liquid and glass state, except for $g_{B-B}(r)$.

The configurations of the two systems at the end of annealing are shown in Fig. 1(f). Compared to the well-mixed glassy state of the KA model, the MKA sample shows a clear phase separation of *A* and *B* particles. In the separated phases, the *A* particles form the fcc phase, while the *B* particles are in the bcc (*B2*) phase.

It is interesting to note that there is almost no difference of atomic diffusivities between the two systems, as shown in Fig. 2. The diffusion constants of KA and MKA at different

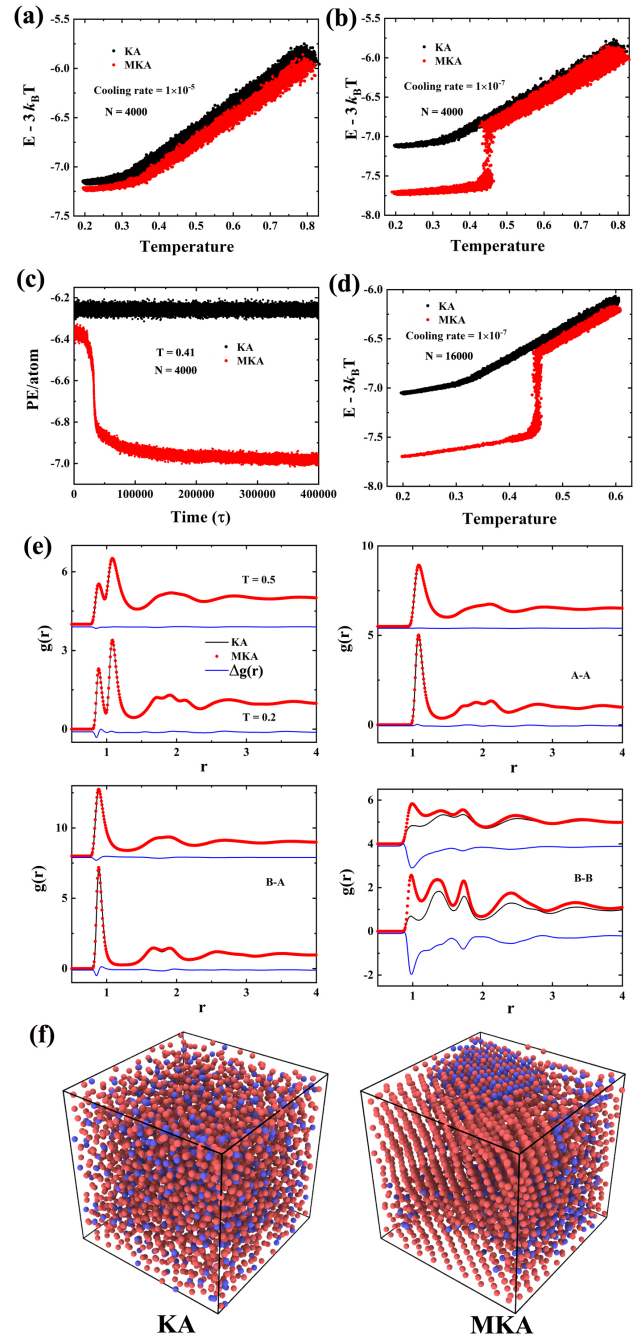


FIG. 1. (a) The instantaneous potential energy ($\text{PE} = E - 3k_B T$)/atom as a function of temperature for KA (black dots) and MKA (red dots), cooling rate = 1×10^{-5} , $N = 4000$. (b) The instantaneous potential energy per atom as a function of temperature for KA and MKA, cooling rate = 1×10^{-7} , $N = 4000$. (c) The potential energy per atom as a function of time for KA and MKA under annealing. (d) The instantaneous potential energy per atom as a function of temperature for KA and MKA; cooling rate = 1×10^{-7} , $N = 16\,000$. (e) The total and partial PCFs for KA (black solid line) and MKA (red dots) under different temperatures for the glass samples are obtained using cooling rate = 1×10^{-5} , $N = 4000$. The difference between KA and MKA $g(r)$ were illustrated by the blue solid line. The PCFs were calculated and averaged over 1000 snapshots. (f) The configurations of KA and MKA systems after annealing at $T = 0.41$. The *A* and *B* particles are represented by red and blue spheres, respectively.

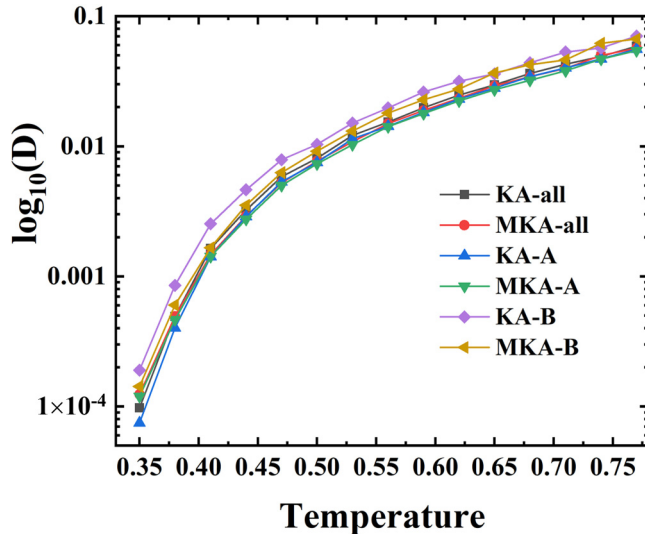


FIG. 2. The atomic diffusion constants (D) for KA and MKA systems at different temperatures. The logarithmic scale for the y axis is adopted to demonstrate the dependence of D on temperature more clearly.

temperatures are fitted from mean-square displacements. The two systems exhibit similar atomic diffusivities at all temperatures, which suggests that the great difference in GFA between KA and MKA cannot be explained in terms of liquid kinetics [30–33]. The relative stability of the stable crystals (convex hull) in KA and MKA [34,35] and the atomic packing efficiency of KA and MKA glasses [36] are also very close to each other (see the Supplemental Material [37] for more details). Hence there must be other underlying factors controlling the GFA in the two systems.

Since the PCF presents only the one-dimensional (1D) averaged features of the 3D atomic structure, a more detailed structural analysis is needed to gain more clear insight into the SRO and MRO in the liquids and glasses to explain the significant difference in the GFA of the two systems. Using the recently developed cluster-alignment method [27,28], together with the clique analysis method [28], we find that the dominant SRO in both KA and MKA glass are B -centered Frank-Kasper Z10 and Z9 [16,38]. Note that Z10 and Z9 motifs are very similar, differing by only one neighbor atom (see Fig. S6 in the Supplemental Material [37]). The polyhedral distortion is a natural way to release the local strain in glass samples, thus Z9 can be identified as a quasiequivalent cluster of Z10. By extending the alignment to medium range, we further show that the Z10 (Z9) clusters with no clear fivefold symmetry are actually covered by a pentagon-dominated second shell to form a unique MRO. In Figs. 3(a) and 3(b), we present the superposed clusters after alignment for the KA and MKA glasses; the A and B particles and the first and second atomic shells are shown separately. The chemical order analysis for SRO and MRO is performed using the superposed clusters. Obviously, the chemical order for SRO is strong for both systems, and the chemical order on the second shell is less pronounced. By calculating the fraction of A particles on each site, we obtain the chemical order for both systems. In KA, the Z10 clusters are in $A_{10}B_1$, while in

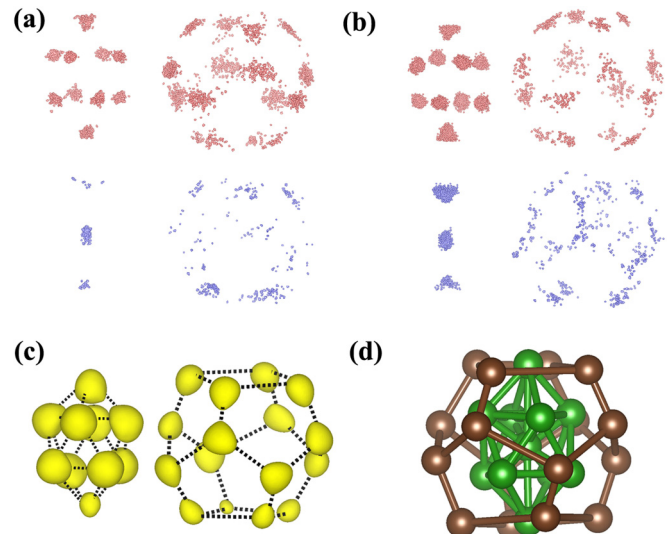


FIG. 3. The superposed clusters after alignment for (a) KA and (b) MKA system. A and B particles are represented by the red and blue dots. (c) The atomic densities of the first and second atomic shells for the superposed clusters. (d) The atomic structure of MRO in the KA and MKA systems. For clarity, the atoms were colored according to their atomic shell instead of chemical species.

MKA, they become $A_{9.33}B_{1.67}$. The A - B bonds are typically shorter than A - A , thus causing the shift of the PCF of MKA, as illustrated in Fig. 1(e). The chemical composition of the second shell of the two systems is A_4B_1 , the same as the system composition, which suggests the absence of chemical ordering. Therefore, the SRO in the two systems shows essentially the same geometric topology and chemical ordering. Figure 3(c) shows the atomic density distribution obtained via a Gaussian smearing method based on the aligned clusters. The local maxima of the atomic densities, which represent the most general pattern shared by the aligned clusters, can then be extracted as the atomic positions, as shown in Fig. 3(d). Previous studies have identified the role of fivefold symmetry in suppressing crystallization [39] and sluggish dynamics in glass-forming undercooled liquids [40]; however, such explanations are unpersuasive for systems where the fivefold symmetry is not the dominant SRO. Here, by unraveling the MRO in KA glass, we show that the fivefold symmetry can emerge in the MRO region, suggesting the critical role of fivefold symmetry.

In Figs. 4(a) and 4(b), we present the temperature dependence of SRO and MRO development with respect to the liquid state in the KA and MKA systems. We use the fractions of atoms involved in the SRO/MRO network as an indicator of the SRO/MRO development. Three temperature regions are identified according to the development of the SRO network; that is, we consider the temperature range where the fraction of atoms included in the SRO network is a plateau as the liquid region, the temperature range where the fraction of atoms in the SRO network starts to grow until it reaches another plateau as the undercooling region, and the remaining temperature range as the glass region. The three temperature windows were highlighted using different colors. To better observe the growth trend, the average fractions in the liquid region

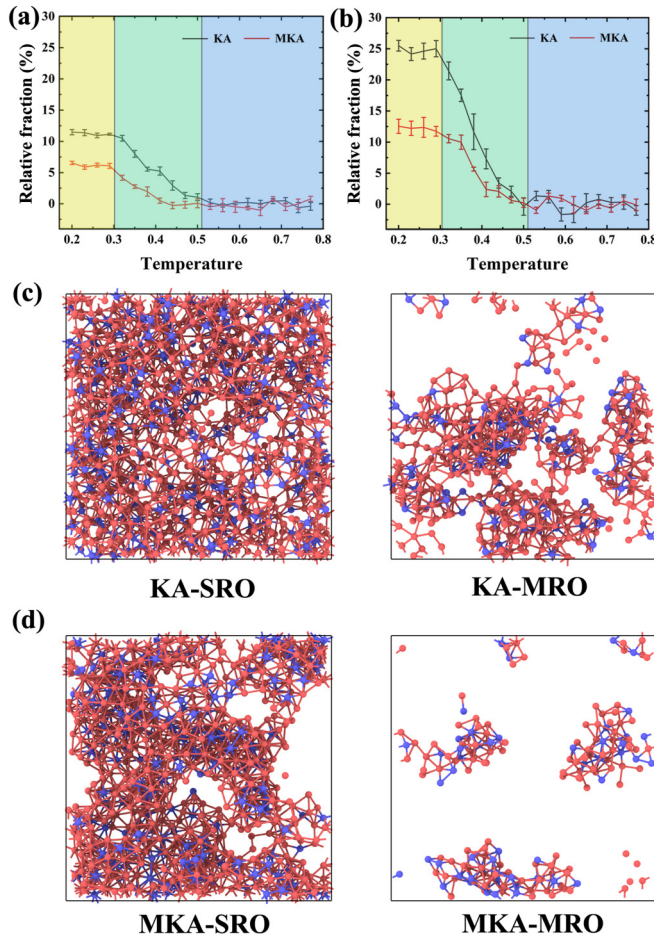


FIG. 4. (a), (b) The relative fractions of atoms included in the SRO and MRO network with respect to that of the liquid state; the liquid, undercooling, and glass regions were highlighted using different colors. The data were averaged over five independent runs, with the error bar denoting the standard deviation. (c), (d) Two slabs with thickness of 3σ for the SRO and MRO percolated network from KA and MKA glass. The A and B particles are colored in red and blue, respectively.

were adopted as references. One can see that the SRO growth behavior in the KA and MKA system are close to each other throughout the three temperature regions. In the glass state, the relative fraction growth with respect to the liquid state for SRO is around 12% and 6% for KA and MKA, respectively. Compared to SRO growth, the difference in relative MRO growth in KA and MKA is roughly doubled. In the glass state, about 26% and 12% more atoms are developed into the MRO network for KA and MKA, respectively. The resulting SRO and MRO networks in the glass state are shown in Fig. 4(c) for the KA system and Fig. 4(d) for the MKA system, respectively. As expected, the percolated SRO networks in both the KA and MKA systems are extended in the whole glass model, while the MRO network in KA glass is much denser than that of MKA glass. Both the decrease in the SRO network and the MRO network density can deteriorate the glass stability. However, the difference in MRO relative density between KA and MKA is about twice that of SRO; thus our results here suggest that the MRO structures with

fivefold symmetries may contribute more to the glass stability, and the percolation may also be involved.

We now further investigate the underlying mechanism of such MRO differences in the two systems and the role of MRO in promoting the GFA. The potential energies of the particles can be obtained by calculating their interactions with all the other atoms in the system. The resulting potential energy distributions of the B atoms centered by the SRO/MRO environment are presented in Fig. 5, in comparison with the B atoms without the SRO/MRO in the samples. The potential energies of the B particles were computed by calculating their interactions with all other atoms in the simulation. It can be seen from Fig. 5(a) that the potential energies of the B atoms with SRO packing in KA are clearly lower than those without the SRO environment, while in MKA, the SRO packing is only slightly favored. Similar results are also observed in the MRO packing environment, as shown in Fig. 5(b). The lower potential energies for B atoms with SRO/MRO packing in KA indicate that both SRO packing and MRO packing are more comfortable packing motifs in the KA system, while in the MKA, the SRO and MRO packing is less favored, which only slightly lowers the potential energies. The decrease of MRO population in MKA can be attributed to the chemical order changes in SRO. In KA, only SROs with $A_{10}B_1$ and A_9B_1 compositions show strong second shell MRO structures, while in MKA, the dominant SROs are in $A_{9.33}B_{1.67}$ and $A_{8.67}B_{1.33}$ compositions. The increased number of B-B bond in the SRO gives rise to a larger distortion of the MRO shell due to the typically shorter B-B bonds, therefore suppressing the MRO formation in the MKA sample.

Previous studies observed that the crystallization of the KA system starts with the formation of pure-A nuclei [29], while in the crystallized MKA system, we also observe a pure-A crystal and an AB B2 region, as can be seen from Fig. 1(f). Hence it is interesting to explore how the phase decomposition is related to the MRO and whether the crystallization process in the MKA system is the same as that of KA. To quantify the degree of phase separation, we characterize the atomic distribution in the glass states with a Gaussian smearing scheme as

$$D(\vec{r}) = \sum_i \left(\frac{1}{2\delta^2\pi} \right)^{3/2} e^{-\frac{(\vec{r}-\vec{r}_i)^2}{2\delta^2}},$$

where \vec{r}_i is the position of atom i . The summation goes over all the atoms in the system, and δ is typically chosen as the location of the first peak in the PCFs. The simulation box is discretized into a $50 \times 50 \times 50$ grid. Figure 6 shows the local density distribution of B in KA and MKA glass with the dashed line indicating the average B density in the two systems. It can be seen that the peak of local density distribution of B in KA is around the system average and the half width is about 0.08, while in MKA the peak is around 0.12 and the distribution is much broader and nonsymmetric, suggesting a heterogeneous distribution of B atoms in the MKA glass. The heterogeneous distribution of B particles can be seen from the B-B partial PCF too, as illustrated in Fig. 1(e). The inset of Fig. 6 shows two cross sections of B-atomic densities in KA and MKA glasses. According to the scale bar, the spatial scale of the density fluctuation is around 4. The B-particle

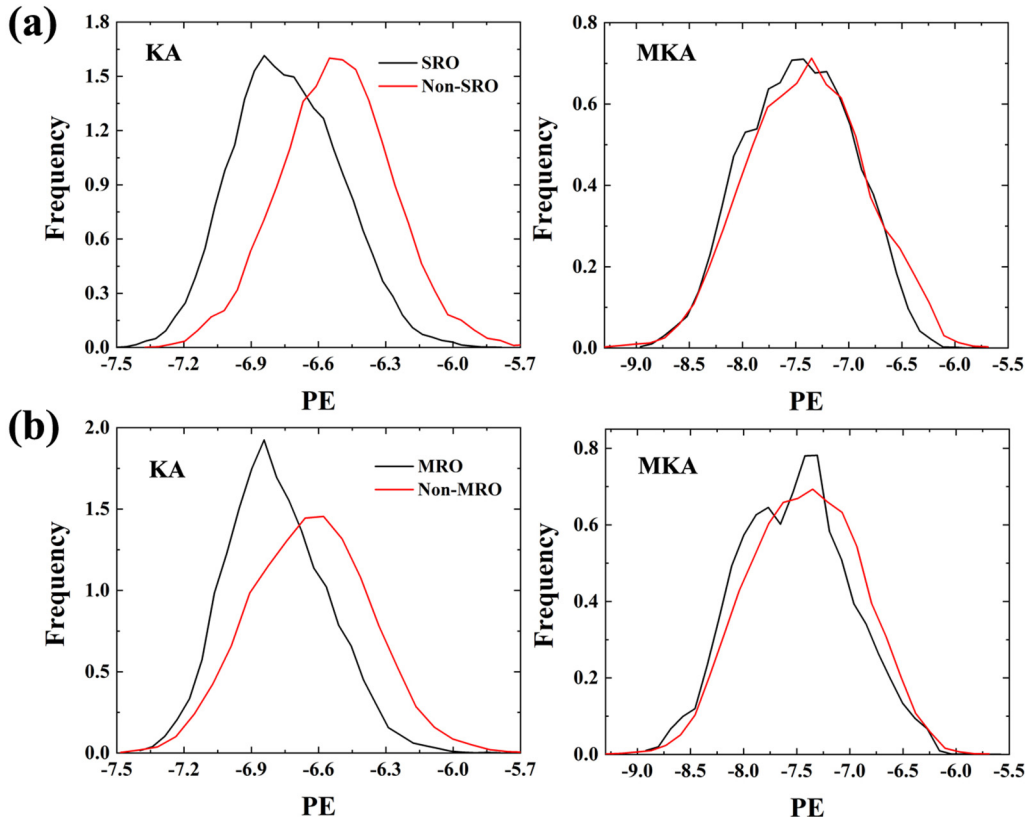


FIG. 5. (a) The distributions of the potential energies of the central B atoms with (black) and without (red) SRO for KA (left) and MKA (right); (b) the same as (a) for B atoms with and without MRO packing. The data were collected from five independent runs.

distribution in KA is almost homogeneous, while there are many B -rich and B -poor regions in MKA, indicating that the phase-decomposition trend is much stronger in MKA. Since

we have shown that the MRO packing in the MKA system is relatively weak due to its energy close to the disordered state in Fig. 5, we can conclude that the lack of MRO fails to block the drift of B particles, and the enriched B - B bonds would further suppress the formation of MRO in the MKA system. Also, the rich MRO in the KA system indicates that more B particles are trapped in the center of a large pentagon-rich cage as compared to that in MKA, and the percolated MRO in KA glass is well extended, leading to an even distribution of particles.

Next, we show that the phase decomposition further promotes the crystal nucleation in MKA. We take a closer inspection of the nucleation process in a slab of a MKA system during the annealing at $T = 0.41$ in Fig. 7. The cluster-alignment method was employed to monitor the change of local crystalline structures [28]. By checking the local crystalline population every 100τ , we found that the nucleus emerges at $t = 69\,000\tau$ for this MKA glass sample; thus a short time period of 400τ before nucleation was adopted for monitoring the growth of the nucleus. Note that the nucleation time would be different for MKA glass samples obtained from a different thermal history. As can be seen from Fig. 7, at $t = 68\,600\tau$, the most pronounced local crystalline order is hcp; only a small portion of atoms are in bcc or fcc. Moreover, the B -rich region indicated by the corresponding atomic density shows no significant difference compared to other regions. After 200τ , some atoms have rearranged into the bcc packing, showing some signals of nucleation in the B -rich region, while the number of atoms in hcp and fcc

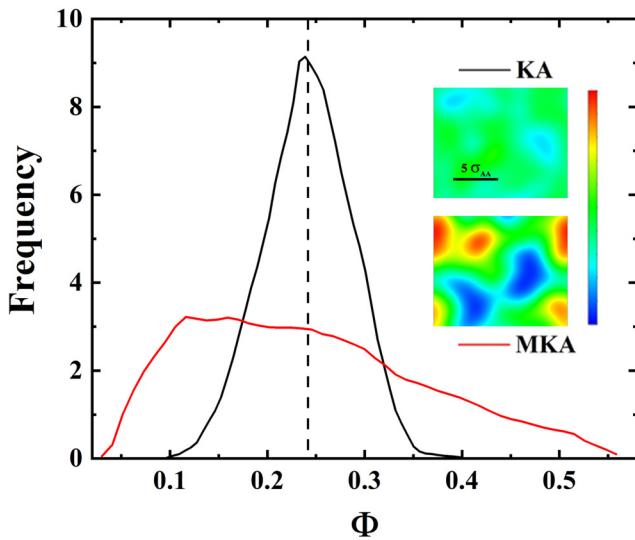


FIG. 6. Local density distribution of B in KA (black) and MKA (red) glass. The dashed line indicates the average B density in the two systems. The inset shows the cross sections of B -atomic density from KA (upper) and MKA (lower) glass. The scale of the inset is in arbitrary units. A scale bar of 5 was attached for measuring the density fluctuation spatial scale.

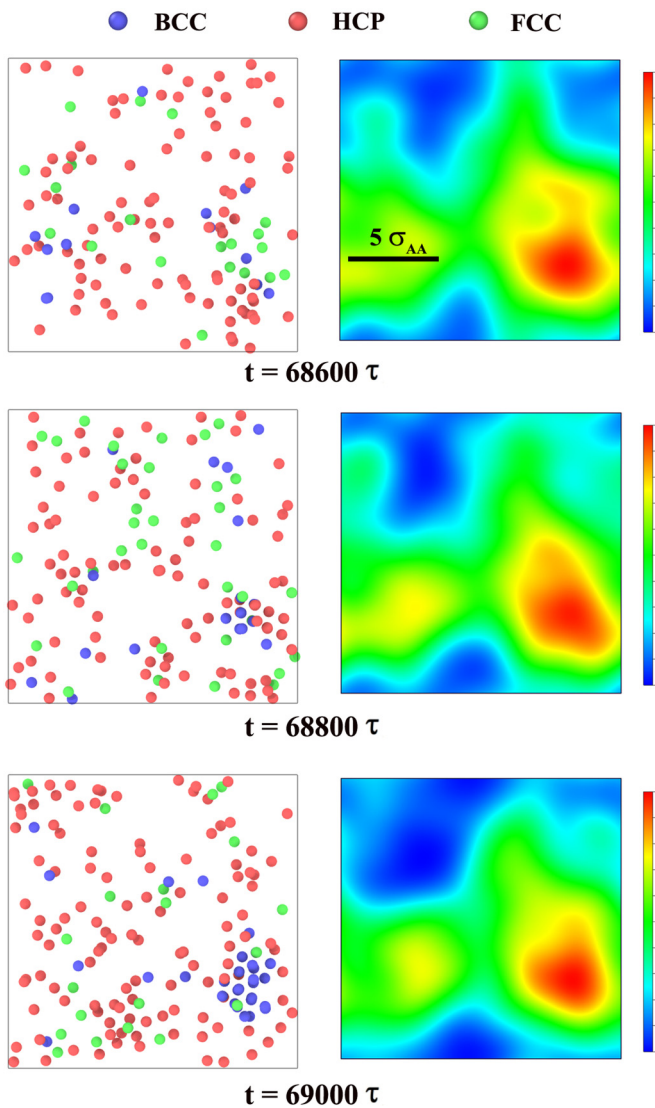


FIG. 7. Three slabs with thickness of 3σ from the MKA system at different annealing times and the corresponding cross sections of B-atomic density. Only the local crystalline orders are shown; the atoms in bcc, hcp, and fcc packing are colored blue, red, and green, respectively. A scale bar of 5 was attached for measuring the density fluctuation spatial scale.

packing still show no significant changes. The bcc nucleus at the B-rich region grows even bigger after some time, as illustrated by the slab at $t = 69\,000\tau$. Further analysis show that this nucleus is in $B2$, consistent with the convex hull of crystal phases (Fig. S1 in the Supplemental Material [37]). In comparison, it has been shown in the literature that the nucleus in KA is in pure A [29], suggesting that the nucleation in KA is also aided by the composition change. Nevertheless, at higher B concentrations ($>40\%$), the $B2$ nucleus in KA can form

instead [41,42]. The crystallization of KA and MKA therefore is promoted in both by the composition changes; however, due to the different development degree of MRO, the two systems show different crystallization paths.

Several factors have been proposed to be responsible for the stabilities of KA glass in the literature, including the structure difference of the dominant SRO in liquid and crystal [41], the order competition between bcc and fcc [43], and the high demixing entropy [44]. Here we give some insight from the MRO perspective. The abundant pentagon-rich MRO in KA glass poses a high-energy barrier for a bcc ($B2$) seed to grow, as reported by Nandi *et al.* [44]. As a result, the crystallization in the KA system can only happen with the help of other types of nuclei. Therefore, it is the pure-A crystal with marginal energy gain serving as the nucleus in KA, because B particles are trapped in the pentagon-rich MRO cages. Hence in larger systems that facilitate the composition fluctuation, the crystallization of KA becomes easier [29], while in the MKA system, the lack of MRO allows the atoms to rearrange easily. Under annealing, once a region with an A/B ratio close to 1 has been formed during compositional fluctuation, it can easily become a $B2$ nucleus with the largest free energy gain such that the crystallization of the MKA system is much easier than that of KA.

IV. CONCLUSION

In summary, we have extracted the exact form of MRO in the KA system, which has fivefold symmetry well beyond the first shell. The MRO in the KA system is found to be responsible for the glass formability and stability in two perspectives: (1) The formation of the $B2$ nucleus is hindered by the MRO cage; (2) the percolated MRO suppressed the composition change in the system. Hence, the effect of MRO must be taken into consideration in glass studies.

ACKNOWLEDGMENTS

Work at SUSTech was supported by the National Natural Science Foundation of China under Grant No. 11774142, and the Shenzhen Basic Research Fund under Grants No. JCYJ20170817105132549, No. JCYJ20180504165817769, and No. JCYJ20170817105201098. The computer time was supported by the Center for Computational Science and Engineering of Southern University of Science and Technology. Work at Ames Laboratory was supported by the US Department of Energy, Office of Science, Basic Energy Sciences, Division of Materials Science and Engineering, including the computer time support on National Energy Research Scientific Computing Center (NERSC) in Berkeley, CA. Ames Laboratory is operated for the US DOE by Iowa State University under Contract No. DE-AC02-07CH11358.

-
- [1] C. P. Royall and S. R. Williams, *Phys. Rep.* **560**, 1 (2015).
[2] D. Wei, J. Yang, M.-Q. Jiang, L.-H. Dai, Y.-J. Wang, J. C. Dyre, I. Douglass, and P. Harrowell, *J. Chem. Phys.* **150**, 114502 (2019).
[3] F. C. Frank, *Proc. R. Soc. London, Ser. A* **215**, 43 (1952).
[4] G. Wahnström, *Phys. Rev. A* **44**, 3752 (1991).
[5] S. G. Hao, C. Z. Wang, M. Z. Li, R. E. Napolitano, and K. M. Ho, *Phys. Rev. B* **84**, 064203 (2011).

- [6] S. Mossa and G. Tarjus, *J. Chem. Phys.* **119**, 8069 (2003).
- [7] C. P. Royall, A. Malins, A. J. Dunleavy, and R. Pinney, *J. Non-Cryst. Solids* **407**, 34 (2015).
- [8] J. Wang, A. Agrawal, and K. Flores, *Acta Mater.* **171**, 163 (2019).
- [9] J. G. Wang, C. T. Chang, K. K. Song, L. Wang, and Y. Pan, *J. Alloys Compd.* **770**, 386 (2019).
- [10] A. Hirata, P. Guan, T. Fujita, Y. Hirotsu, A. Inoue, A. R. Yavari, T. Sakurai, and M. Chen, *Nat. Mater.* **10**, 28 (2010).
- [11] N. A. Mauro, V. Wessels, J. C. Bendert, S. Klein, A. K. Gangopadhyay, M. J. Kramer, S. G. Hao, G. E. Rustan, A. Kreyssig, A. I. Goldman, and K. F. Kelton, *Phys. Rev. B* **83**, 184109 (2011).
- [12] L. Huang, C. Z. Wang, S. G. Hao, M. J. Kramer, and K. M. Ho, *Phys. Rev. B* **81**, 094118 (2010).
- [13] L. Huang, X. W. Fang, C. Z. Wang, M. J. Kramer, Z. J. Ding, and K. M. Ho, *Appl. Phys. Lett.* **98**, 231906 (2011).
- [14] T. Kawasaki, T. Araki, and H. Tanaka, *Phys. Rev. Lett.* **99**, 215701 (2007).
- [15] T. Kawasaki and H. Tanaka, *J. Phys.: Condens. Matter* **23**, 194121 (2011).
- [16] H. W. Sheng, W. K. Luo, F. M. Alamgir, J. M. Bai, and E. Ma, *Nature* **439**, 419 (2006).
- [17] M. Kbirou, S. Trady, A. Hasnaoui, and M. Mazroui, *Chem. Phys.* **513**, 58 (2018).
- [18] D. Z. Chen, C. Y. Shi, Q. An, Q. Zeng, W. L. Mao, W. A. Goddard, and J. R. Greer, *Science* **349**, 1306 (2015).
- [19] D. Ma, A. D. Stoica, and X. L. Wang, *Nat. Mater.* **8**, 30 (2009).
- [20] S. Trady, M. Mazroui, A. Hasnaoui, and K. Saadouni, *J. Alloys Compd.* **744**, 750 (2018).
- [21] Y. Hiraoka, T. Nakamura, A. Hirata, E. G. Escolar, K. Matsue, and Y. Nishiura, *Proc. Natl. Acad. Sci. USA* **113**, 7035 (2016).
- [22] F. Zhang, M. I. Mendelev, Y. Zhang, C.-Z. Wang, M. J. Kramer, and K.-M. Ho, *Appl. Phys. Lett.* **104**, 061905 (2014).
- [23] H. Staley, E. Flennner, and G. Szamel, *J. Chem. Phys.* **145**, 184505 (2016).
- [24] A. Foroughi, R. Tavakoli, and H. Aashuri, *J. Non-Cryst. Solids* **481**, 132 (2018).
- [25] W. Kob and H. C. Andersen, *Phys. Rev. E* **51**, 4626 (1995).
- [26] lammps.sandia.gov/.
- [27] X. W. Fang, C. Z. Wang, Y. X. Yao, Z. J. Ding, and K. M. Ho, *Phys. Rev. B* **82**, 184204 (2010).
- [28] Y. Sun, F. Zhang, Z. Ye, Y. Zhang, X. Fang, Z. Ding, C. Wang, M. I. Mendelev, R. T. Ott, M. J. Kramer, and K. Ho, *Sci. Rep.* **6**, 23734 (2015).
- [29] T. S. Ingebrigtsen, J. C. Dyre, T. B. Schröder, and C. P. Royall, *Phys. Rev. X* **9**, 031016 (2019).
- [30] Z. Ye, F. Zhang, Y. Sun, M. C. Nguyen, S. H. Zhou, L. Zhou, F. Meng, R. T. Ott, E. Park, M. F. Besser, M. J. Kramer, Z. J. Ding, M. I. Mendelev, C. Z. Wang, R. E. Napolitano, and K. M. Ho, *Phys. Rev. Materials* **1**, 055601 (2017).
- [31] J. Russo, F. Romano, and H. Tanaka, *Phys. Rev. X* **8**, 021040 (2018).
- [32] C. Tang and P. Harrowell, *Nat. Mater.* **12**, 507 (2013).
- [33] Y. Sun, F. Zhang, L. Yang, H. Song, M. I. Mendelev, C.-Z. Wang, and K.-M. Ho, *Phys. Rev. Mater.* **3**, 023404 (2019).
- [34] D. M. Deaven and K. M. Ho, *Phys. Rev. Lett.* **75**, 288 (1995).
- [35] S. Q. Wu, M. Ji, C. Z. Wang, M. C. Nguyen, X. Zhao, K. Umemoto, R. M. Wetzcovitch, and K. M. Ho, *J. Phys.: Condens. Matter* **26**, 035402 (2014).
- [36] L. Ward, D. Miracle, W. Windl, O. N. Senkov, and K. Flores, *Phys. Rev. B* **88**, 134205 (2013).
- [37] See Supplemental Material at <http://link.aps.org/supplemental/10.1103/PhysRevB.101.214104> for comparisons of liquid kinetics, convex hull between the KA and MKA system, atomic packing efficiency, and the details for extracting the SRO and MRO; also see Refs. [30–36].
- [38] F. C. Frank and J. S. Kasper, *Acta Crystallogr.* **11**, 184 (1958).
- [39] J. Taffs and C. Patrick Royall, *Nat. Commun.* **7**, 13225 (2016).
- [40] Y. C. Hu, F. X. Li, M. Z. Li, H. Y. Bai, and W. H. Wang, *Nat. Commun.* **6**, 8310 (2015).
- [41] A. Banerjee, S. Chakrabarty, and S. M. Bhattacharyya, *J. Chem. Phys.* **139**, 104501 (2013).
- [42] U. R. Pedersen, T. B. Schroder, and J. C. Dyre, *Phys. Rev. Lett.* **120**, 165501 (2018).
- [43] J. R. Fernandez and P. Harrowell, *Phys. Rev. E* **67**, 011403 (2003).
- [44] U. K. Nandi, A. Banerjee, S. Chakrabarty, and S. M. Bhattacharyya, *J. Chem. Phys.* **145**, 034503 (2016).

Supplemental Material for:

**Unveiling the medium-range order in the glass models and its role in glass
formation**

Xinyu Fan^{1,2}, Yang Sun^{3,4}, Cai-Zhuang Wang^{3*}, Kai-Ming Ho³, M. S. Altman²,
and Li Huang^{1*}

¹*Department of Physics, Southern University of Science and Technology,
Shenzhen, Guangdong 518055, China*

²*Department of Physics, Hong Kong University of Science and Technology,
Clear Water Bay, Kowloon, Hong Kong SAR, China*

³*Ames Laboratory, U.S. Department of Energy and Department of Physics, Iowa
State University, Ames, Iowa 50011, USA*

⁴*Department of Applied Physics and Applied Mathematics, Columbia University,
New York, New York 10027, USA*

*Corresponding author: huangl@sustech.edu.cn; wangcz@ameslab.gov

The devitrification of glasses is associated with many factors, including but not limited to the free energy change, the structural difference between amorphous and crystal state, the atomic diffusivity, the solid-liquid interface energy [30-33]. Here we'll examine some of these factors in KA and MKA systems. The strategy for extracting the short-range order and medium-range order and chemical order in glassy systems from scratch was also discussed in detail.

The convex hull

Fig. S1 illustrates the convex hulls of KA and MKA system. The genetic algorithm implemented in GA code was adopted to search for low energy KA and MKA crystal structures [34, 35]. The formation energies are calculated with respect to A, B FCC crystals. One can see that the global minimum crystal of both KA and MKA system is in equimolar B2 (CsCl) phase, and the convex hulls of the two systems are close to each other.

Fig.S1 X. Fan et al.

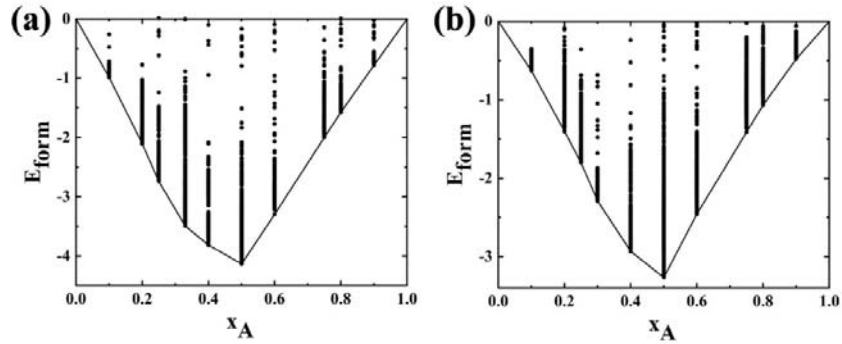


Fig. S1 The convex hull of (a) KA system and (b) MKA system.

The SRO in glass and structural difference between glass and crystal

Next, we proceed to check the similarity between dominant short-range order (SRO) and the crystal structure building blocks for the two systems. To do this, we need to extract the dominant SRO first. Here we show the procedures using KA system as an example.

Fig.S2 X. Fan et al.

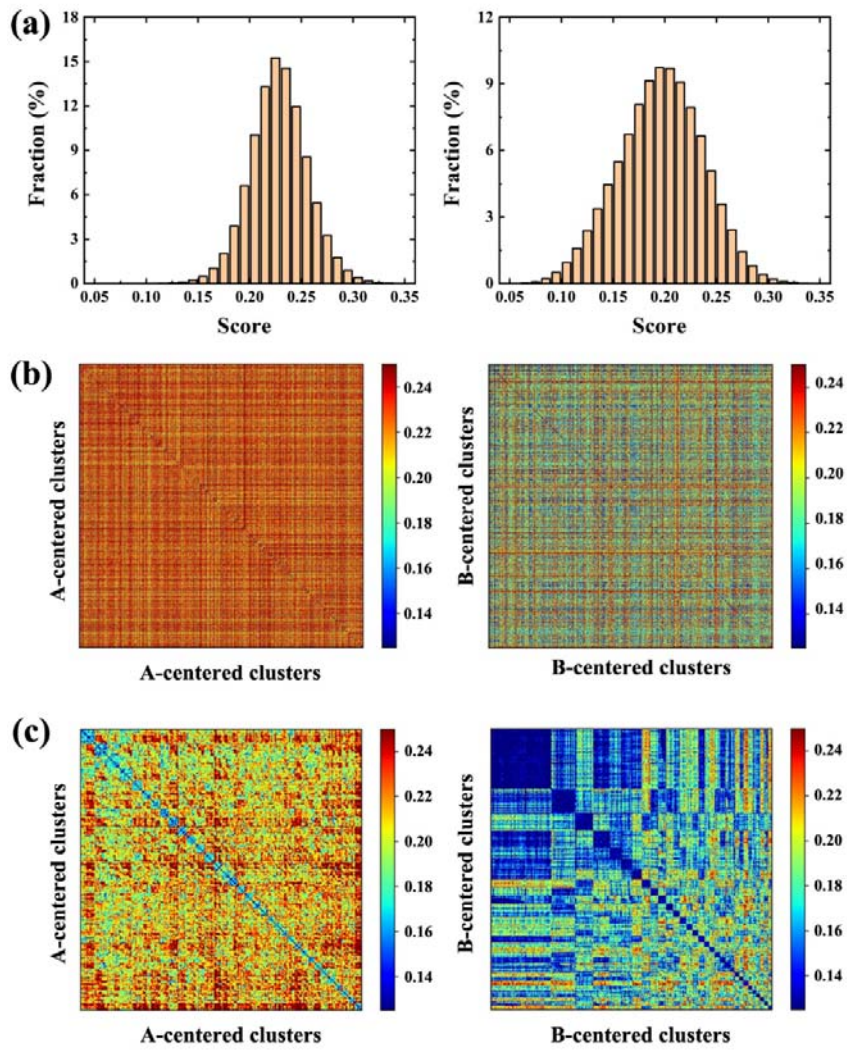


Fig. S2 Pair-wise alignment results for A- and B-centered clusters. (a) score distribution of A-centered clusters (left) and B-centered clusters (right). (b) Similarity matrix for A- and B-centered clusters. (c) Similarity matrix for A- and B-centered clusters after clique analysis. The color bars indicate the alignment scores.

By integrating the pair-correlation functions (Fig. 1(e) in the main text) to its first minimum, we can obtain the number of nearest neighbors for both A and B atoms. The number of nearest neighbors for A and B are found to be 13.8 and 9.4 respectively. Then 1,000 A- and B-centered clusters were chosen at random to perform the pair-wise alignment. The number of atoms in the clusters are slightly

larger than the number of nearest neighbors to ensure that the SRO has been covered.

The similarity between two clusters is measured using the alignment score

$$\text{score} = \min\left(\frac{1}{N} \sum_{i=1}^N \Delta r^2\right)^{1/2}$$

where N is the number of atoms in the template cluster, Δr is the deviation between individual atoms in the template cluster and the target cluster, a smaller score indicates a lower deviation between the clusters. In Fig. S2(a), we present the distributions of pair-wise alignment scores for A- and B-centered clusters. The peak of the score distribution of the A-centered clusters is around 0.22, while for B-centered clusters it is around 0.19, indicating an overall larger distortion among A-centered clusters. We use the half-width of the pair-wise alignment score distribution as the score cutoff for A- and B-centered clusters, that is, if the mutual alignment score between two clusters are smaller than the score cutoff, they are considered as identical. Here a cutoff score of 0.19 and 0.15 has been used for A- and B-centered clusters, respectively. we can rearrange the similarity matrix using clique analysis to group the clusters.

The similarity matrix for A- and B-centered clusters before and after rearrangement are shown in Fig. S2(b) and (c). The clique analysis of the similarity matrix of B-centered clusters has identified a largest clique that contains more than 10% of the total clusters, as well as several smaller cliques, indicating the strong SRO in B-centered clusters. While for A-centered clusters, we cannot identify a clique even with significant large size. The above results show that the B-centered clusters dominant the SRO in KA glass. By analyzing the cluster structure within the maxima cliques, we can extract the cluster structure that is most representative among the B-centered clusters. That is, first we superpose the clusters within the clique by overlapping their central atoms, then we can calculate the atomic density using Gaussian smearing. Then, the local density maxima can be used to extract the atomic position. In Fig. S3, we show this process using the clusters from the largest two cliques. We find that the dominant SRO in KA glass is Frank-Kasper Z10 and Z9, the clusters from other cliques are either fragmental or distorted Z10 or Z9. The dominant

SRO in MKA glass is also identified as Z10 and Z9. With the same dominant SRO and similar convex shape of KA and MKA (Fig. S1), one can expect that the structural difference between the glass state and crystal in the two system is identical.

Fig.S3 X. Fan et al.

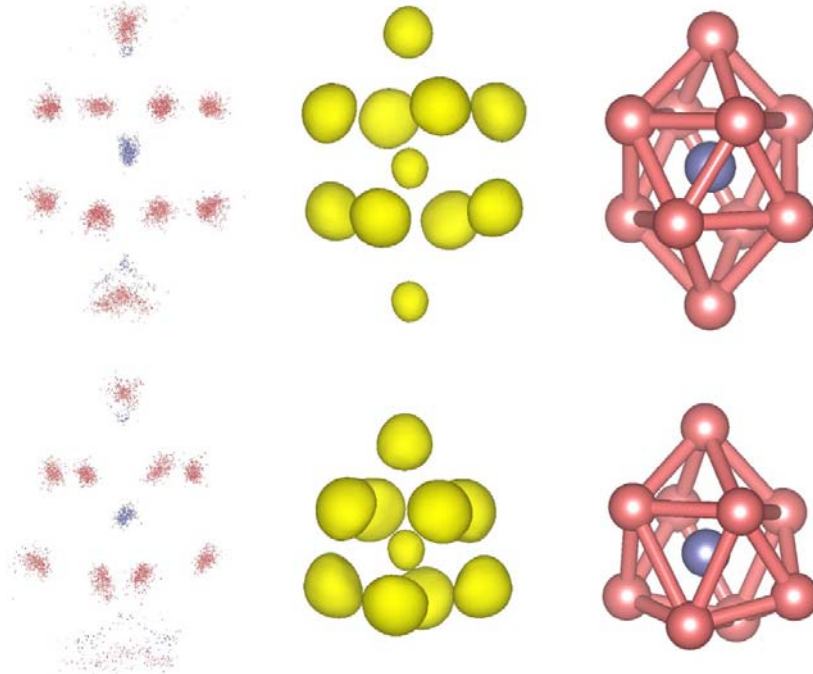


Fig. S3 The superposed clusters from the largest two cliques for KA glass (left); the corresponding atomic-density (middle); and the extracted atomic structure (right). The central B atom is colored in purple, while the surrounding A atoms were colored in red.

The atomic packing efficiency

The atomic packing efficiency (APE) measures how much a cluster packing deviates from the ideal packing [36], which may provide useful insight for studying the difference in GFA between KA and MKA. The parameter is defined as:

$$\text{APE} = \left(\frac{r_0}{r_1}\right)/R^*$$

where r_0 is the radius of the central atom, r_1 is the mean radius of the nearest neighbors, and R^* is the optimal radius ratio for the clusters. The APE of KA and MKA glasses is shown in Fig. S4. As can be seen from Fig. S4, the APE distribution for KA and MKA glasses only show little difference.

Fig.S4 X. Fan et al.

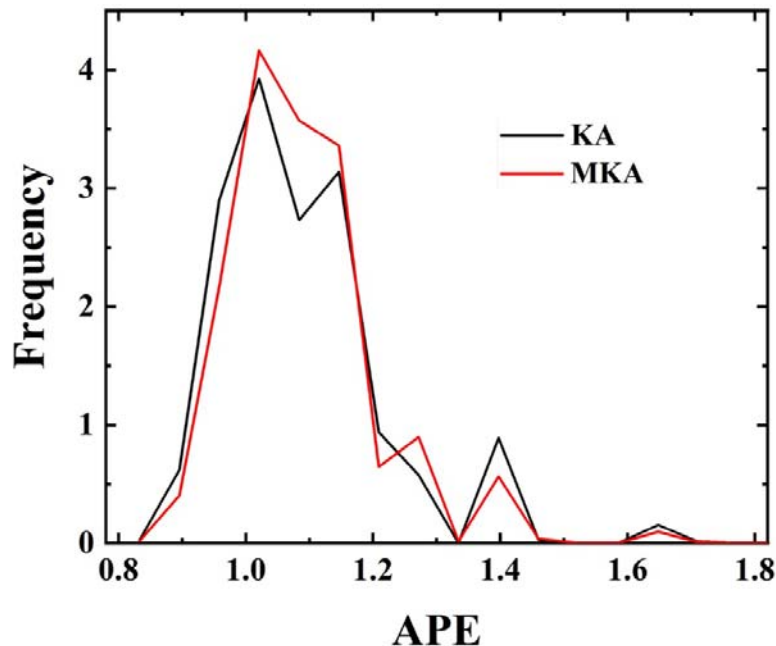


Fig. S4 The atomic packing efficiency distribution for KA and MKA glasses.

The medium-range order

With the resulting dominant SRO, we can perform template alignment using the dominant SRO as templates on larger B-centered clusters (~ 100 atoms), and follow the align-superpose-density procedure, we can extract the MRO structure in the two systems, as shown in Fig. 3 in the main text and Fig. S5 here. The third atomic shell is very weak with the current cooling rate; we thus adopt the second shells as the MRO in the main text.

Fig.S5 X. Fan et al.

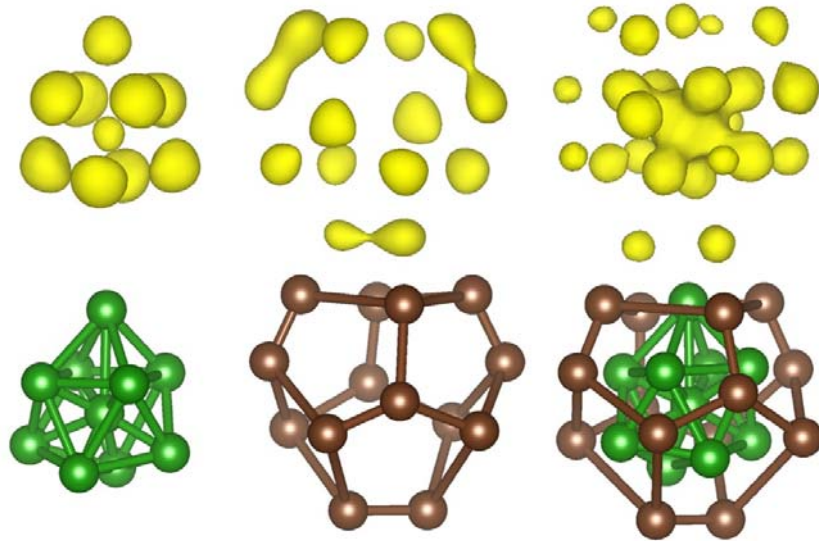


Fig. S5 The first and second shell of Z9 cluster in KA and MKA glass. The inner and outer-shell atoms are colored differently.

The comparison between Z9 and Z10

Fig. S6 shows the superposed Z9 and Z10 cluster after alignment. One can see the two clusters are almost totally overlapped; hence we identify one of Z9 and Z10 is a distorted version of the other, which is a natural way to release local strain. Thus, the Z9 and Z10 are treated as SRO in the main text, and their second shells were treated as MRO.

Fig.S6 X. Fan et al.

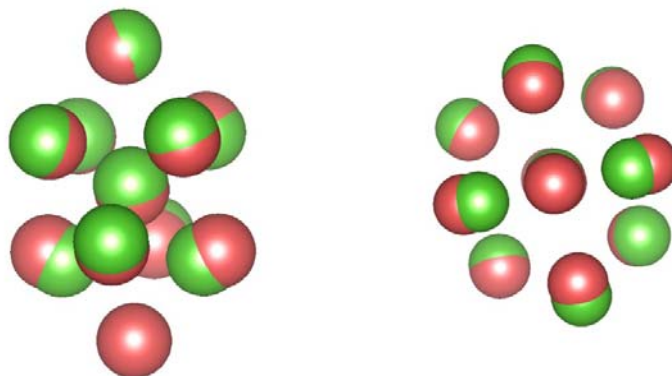


Fig. S6 The superposed Z9 and Z10 cluster, both side view and top view. Z10 was

colored in red, while Z9 was colored in green.